PHYSICAL REVIEW B **76**, 174114 (2007)

Ferroelectric nanoscale domains and the 905 K phase transition in $SrSnO_3$: A neutron total-scattering study

Andrew L. Goodwin, Simon A. T. Redfern, and Martin T. Dove
Department of Earth Sciences, University of Cambridge, Downing Street, Cambridge CB2 3EQ, United Kingdom

David A. Keen
ISIS Facility, Rutherford Appleton Laboratory, Harwell Science and Innovation Campus, Didcot, Oxfordshire OX11 0QX, United Kingdom
and Clarendon Laboratory, Department of Physics, Oxford University, Parks Road, Oxford OX1 3PU, United Kingdom

Matthew G. Tucker
ISIS Facility, Rutherford Appleton Laboratory, Harwell Science and Innovation Campus, Didcot, Oxfordshire OX11 0QX, United Kingdom

(Received 19 July 2007; published 27 November 2007)

The 905 K *Pnma*–*Imma* phase transition in $SrSnO_3$ is studied here using a combination of variable-temperature neutron total scattering together with the reverse Monte Carlo (RMC) refinement method. The real-space RMC configurations obtained are analyzed in terms of bond distance and bond-angle distributions, and a geometric algebra approach is used to quantify the associated octahedral-tilting distributions. What emerges from this analysis is that the transition is displacive in nature, in contrast to the results of a recent average-structure investigation in which an order-disorder model was proposed [E. H. Mountstevens *et al.*, Phys. Rev. B **71**, 220102(R) (2005)]. Three-dimensional diffuse scattering patterns calculated from the same RMC configurations reveal the existence of an additional disorder mechanism which persists across the *Pnma-Imma* transition. The "reflection conditions" of this diffuse scattering, together with displacement correlation calculations, point to the existence of ferroelectric nanoscale domains within the configurations, which are found to extend across planar regions of approximately 10–15 Å in diameter.

DOI: 10.1103/PhysRevB.76.174114 PACS number(s): 61.12.−q, 61.50.Ks, 77.80.Dj, 77.84.Dy

I. INTRODUCTION

The family of ABO_3 perovskites is a particularly important class of materials notable for its diversity of physicochemical behavior.[1] Its members include widely studied ferroelectric materials such as $BaTiO_3$, colossal magnetoresistant manganites such as the prototypical $(La,Pr,Ca)MnO_3$ family, and geologically important minerals such as the lower-mantle-forming $MgSiO_3$ perovskite. The lattice dynamics of this broad family are characterized by a number of soft-mode instabilities, reflected in a rich structural behavior with many members exhibiting structural phase transitions in response to changes in temperature, pressure, and composition. Understanding the nature of these phase transitions is central to elucidating the most important atomic-level interactions and processes in these materials.

The two classes of soft-mode transitions—namely, ferroelectric and octahedral tilting—involve mode condensation at different wave vectors ($\mathbf{k}=0$ and $\langle\frac{1}{2}\frac{1}{2}\xi\rangle^*$, respectively), and while some degree of controversy persists concerning the relative dynamic and order-disorder contributions in the ferroelectric case (e.g., the ferroelectric transitions in $BaTiO_3$, see Refs. 2–5), the octahedral-tilting transitions are almost universally considered to be displacive in character.[6,7] In this context, a recent neutron diffraction study of the octahedral-tilting transitions of $SrSnO_3$ was particularly interesting because it suggested that a significant order-disorder contribution may be present in this case.[8]

The compound in question—$SrSnO_3$, a chemical and structural analog of $MgSiO_3$ perovskite (which is thermodynamically unstable at ambient conditions)—is of interest for its attractive dielectric properties,[9] potential application in single flux quantum circuits,[10] ability to sense variations in humidity,[11,12] and its photoluminescence and photocatalytic behaviors.[13] The material exhibits a series of octahedral-tilting transitions when heated, progressing from its room-temperature *Pnma* cell to *Imma* at 905 K, to *I*4/*mcm* at 1062 K, and, finally, to the $Pm\bar{3}m$ aristotype at 1295 K.[8,14] Both differential scanning calorimetry and dilatometric measurements show additional discontinuities at approximately 350 K (Ref. 14); however, no crystallographic evidence of a structural phase transition has been reported at this temperature. This series of transitions is not particularly unusual for perovskite systems: it has also been observed in $SrZrO_3$,[15,16] $SrRuO_3$,[17] and $SrRhO_3$ (Ref. 18) with temperature, and with increasing x in the solid solution $Sr_xBa_{1-x}SnO_3$ at 300 K.[19]

In this paper, we use the experimental technique of neutron total scattering to examine the dynamic and structural behaviors of $SrSnO_3$ across its 905 K *Pnma*–*Imma* transition. Neutron total scattering provides a unique and valuable window into the structural and dynamical behaviors of crystalline materials, particularly when coupled with real-space refinement processes such as the reverse Monte Carlo (RMC) method (described in greater detail below).[20] Its key advantage as a crystallographic technique is that it yields at once both local and average descriptions of the crystal structure. In the context of $SrSnO_3$, this is most relevant because both displacive and order-disorder mechanisms can appear largely indistinguishable in terms of their effects on the average structure, but there is a dramatic change in local structure between the two cases. Indeed, a recent study of the 105 K displacive phase transition in strontium titanate highlighted the reliability with which octahedral-tilting distribution functions—which are diagnostic measures of both dynamic and order-disorder mechanisms—could be determined in this way.[21]

As for a number of previous total-scattering studies of structural phase transitions in crystalline materials (for some examples, see Refs. 21–23), we employ here the RMCPROFILE implementation of the RMC refinement method[20] as a means of analyzing our experimental scattering data. Historically, RMC has been used to model the structures of liquids and amorphous systems,[24] and RMCPROFILE extends this same approach to crystals, where it is especially suited to studying local structure and crystalline disorder. In this case, real-space analysis of the RMC atomistic configurations is found to support a displacive description of the 905 K transition in $SrSnO_3$, with no appreciable order-disorder components. Moreover, and quite separate from the phase transition itself, we find unexpected evidence of polar nanoregions (PNRs) within our RMC configurations. These single-layer ferroelectric domains are found to extend over planar regions approximately 10–15 Å in diameter, and are of interest because their existence may have unforeseen implications for the dielectric properties of the material.

The presence of PNRs at temperatures above the Curie temperature in relaxor ferroelectrics such as $Pb(Zn_{1/3}Nb_{2/3})O_3$ (PZN) and $Pb(Mn_{1/3}Nb_{2/3})O_3$ (PMN) is now generally accepted,[25] as is their important role in relaxor behavior;[26–28] however, the structure and origin of these polar domains remain debated.[29–32] Perhaps the most convincing evidence for their existence and nature is to be found in single-crystal diffuse scattering experiments, where characteristic rodlike streaking across specific regions of reciprocal space is strongly diagnostic of planar ferroelectric displacements.[31,32] A recent bond valence analysis also provides a chemical basis for particular displacement patterns consistent with the diffuse scattering, suggesting that the domains arise so as to optimize local bonding interactions.[32] The approaches taken so far have certainly shown that experimentally determined features such as diffuse scattering patterns are consistent with the proposed PNR models. That similar domains emerge from our RMC analysis of $SrSnO_3$ despite the absence of a preconceived PNR model is an interesting development; the nanodomains simply evolve in the RMC refinement so as to fit the available data as closely as possible. In this way, our $SrSnO_3$ results provide a useful comparison for the perhaps more widely studied PZN and PMN materials.

Our paper begins with a review of the 905 K phase transition in $SrSnO_3$, followed by a description of the experimental and computational techniques used in our analysis. We then report the results of our RMC refinement, including the diagnostic octahedral-tilting distributions extracted using a recently developed approach based on geometric algebra. The emphasis of the paper then shifts to our reciprocal-space and real-space evidence for PNRs in $SrSnO_3$. We conclude with a discussion of the results of our RMC analysis, rationalizing the findings of Ref. 8 in their context and discussing the implications of ferroelectric nanoscale domains on the physical properties of $SrSnO_3$.

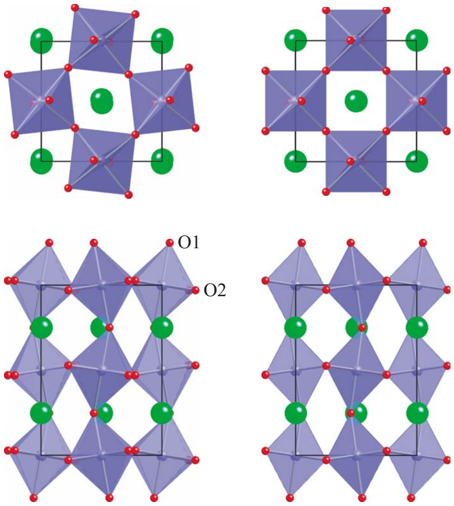

FIG. 1. (Color online) Representations of the *Pnma* (left) and *Imma* (right) crystal structures of $SrSnO_3$, viewed down the crystallographic **b** (top) and **a** (bottom) axes. The transition from *Pnma* to *Imma* involves a loss of the in-phase octahedral-tilt system along **b**. The Sn positions (centers of the octahedra) remain unchanged throughout the transition.

II. 905 K PHASE TRANSITION IN STRONTIUM STANNATE

The transition in $SrSnO_3$ between *Pnma* ($a^+b^-b^-$; Ref. 33) and *Imma* ($a^0b^-b^-$) phases—first reported only very recently[14]—corresponds to the loss of an in-phase octahedral-tilt system parallel to the **b** crystal axis (Fig. 1). In contrast, the out-of-phase tilt system parallel to **a** remains in both phases.[34] Both *Pnma* and *Imma* unit cells are related to the parent cubic perovskite structure via the same transformation

$$\begin{bmatrix}\mathbf{a}\\ \mathbf{b}\\ \mathbf{c}\end{bmatrix}_{Pnma/Imma} = \begin{bmatrix}1 & 0 & -1\\ 0 & 2 & 0\\ 1 & 0 & 1\end{bmatrix} \times \begin{bmatrix}\mathbf{a}\\ \mathbf{b}\\ \mathbf{c}\end{bmatrix}_{Pm\bar{3}m} \tag{1}$$

and so there is no change in metric associated with the transition. The two phases also contain the same number of crystallographically distinct atoms; in particular, each cell contains two distinct types of oxygen atom, which correspond to apical (O1) and equatorial (O2) octahedral vertices relative to the crystal **b** axis (see Fig. 1). The generalized atomic coordinates for each of the two unit cells are listed in Table I.

Because the transition is continuous, the magnitude of the associated octahedral-tilt angle is a measure of the order parameter. This angle is reported to decrease smoothly with heating from a value of 6.89° (Ref. 8) or 6.2° (Ref. 14) at room temperature to 0° at 908.6(6) K (Ref. 8) or 905 K.[14] This is actually a reasonably large change in tilt angle for a continuous transition; cf. the change in tetrad tilt angle of ~2° in the well-known $I4/mcm$–$Pm\bar{3}m$ transition of

TABLE I. Atomic coordinates (x,y,z) for the *Pnma* and *Imma* phases of $SrSnO_3$.

	Pnma	*Imma*
Sr	$(\delta_{x\mathrm{Sr}},0.25,z)$	$(0,0.25,z)$
Sn	(0, 0, 0.5)	(0, 0, 0.5)
O1	$(0.5-\delta_{x\mathrm{O1}},0.25,z)$	$(0.5,0.25,z)$
O2	$(0.25+\delta_{x\mathrm{O2}},y,0.75-\delta_{z\mathrm{O2}})$	$(0.25,y,0.75)$

$SrTiO_3$.[35] The order parameter was reported to vary with temperature according to a critical exponent of $\beta=0.187$,[8] which is substantially lower than that expected for a second-order ($\beta=0.5$) or a tricritical ($\beta=0.25$) displacive phase transition, but similar to the values observed in some order-disorder transitions.[36–38] This observation led Mountstevens *et al.* (including one of us, namely, S.A.T.R.) to interpret the transition in terms of an order-disorder model,[8] in which both *Pnma* and *Imma* phases were described by a superposition of two sets of atomic positions—one for each of the possible directions of the *Pnma* in-phase tilting distortion. The populations p and $1-p$ of these two sets were constrained to be equal in the *Imma* regime, whereas the value p was included as a refinable parameter for the *Pnma* phase. Using this approach, the octahedral-tilt angle was found to decrease much more conservatively with increasing temperature, remaining significant at T_c. A small amount of critical behavior was still observed, and its relative magnitude suggested that the transition might be predominantly ($\simeq 75\%$) order-disorder in nature.

Distinguishing between order-disorder and displacive mechanisms is inherently difficult when using average-structure techniques because the distinction lies in the way local bonding environments are affected by the phase transition. The feature of local structure that would be highly diagnostic of a disordered *Imma* phase is the distribution of octahedral-tilt angles θ relative to the **b** crystallographic axis. Should the octahedral geometry be preserved, a standard displacive model of the transition would be reflected in a tilt distribution with a single maximum at $\theta=0$; a disorder model requires a symmetric bimodal distribution with maxima at $\pm\theta\neq 0$. In this case, the average-structure analysis of Ref. 8 would suggest the maxima to occur at tilt angles of approximately ±5.3° at 930 K. The experimental distribution may be obtained via real-space analysis of neutron total-scattering data, and is one of the key issues to be explored in our study.

III. METHODS

A. Neutron total-scattering data collection

The neutron time-of-flight diffractometer GEM[39–41] at the ISIS pulsed spallation source was used to collect total-scattering patterns from a polycrystalline $SrSnO_3$ sample, prepared by sintering a mixture of $SrCO_3$ and SnO_2 at 1830 °C. Data were collected over a large range of scattering vectors of magnitudes $0.3\leqslant Q\leqslant 50$ Å^{-1}, giving a real-space resolution of order $\Delta r\simeq 3.791/Q_{\max}\simeq 0.08$ Å. For the experiment, approximately 6 g of sample was placed within a cylindrical vanadium can of 8 mm diameter and 5.8 cm height. This was mounted within a custom-designed furnace. Extended data collections suitable for subsequent RMC analysis were performed at temperatures of 500, 750, 800, 850, and 930 K.

Following their collection, the total-scattering data were corrected using standard methods, taking into account the effects of background scattering, absorption, multiple scattering within the sample, and beam intensity variations, and the Placzek inelasticity correction was applied.[42] These corrected data were then converted to experimental $F(Q)$ and $T(r)$ functions,[42,43] which are related to the radial distribution function $G(r)$ by the equations

$$F(Q)=\rho_0\int_0^\infty 4\pi r^2 G(r)\frac{\sin Qr}{Qr}dr, \tag{2}$$

$$T(r)=4\pi r\rho_0\left[G(r)+\left(\sum_m c_m b_m\right)^2\right], \tag{3}$$

where ρ_0 is the number density, c_m the concentration of each species m, and b_m the corresponding neutron scattering lengths. The Bragg profiles for each data set were extracted from the scattering data collected by the detector bank centred on $2\theta=63.62°$. These profiles were fitted using the GSAS structural refinement program,[44] and the structural models produced were verified against previously published data, using an ordered *Imma* model for the 930 K data.[8,14]

B. Reverse Monte Carlo refinement

The reverse Monte Carlo refinement method and its implementation in the program RMCPROFILE have been described in detail elsewhere.[20,42] The basic refinement objective is to produce atomistic configurations that account simultaneously for the experimental $F(Q)$, $T(r)$, and Bragg profile functions. This is achieved by accepting or rejecting random atomic moves subject to the metropolis Monte Carlo algorithm, where in this case the Monte Carlo energy function is determined by the quality of the fits to the data.

For the present study, starting configurations for the RMC process were produced from $8\times 6\times 8$ supercells of the crystallographic unit cell determined in the GSAS refinements described above. These supercells contained 7680 atoms, and were chosen to be roughly equivalent in length along each axis (about 45 Å). Small random initial displacements were applied to all atoms, and a set of data-based "distance window" constraints were applied in order to maintain an appropriate framework connectivity throughout the refinement process.[20,45] The values used for these constraints are given in Table II, where they are shown not to interfere with the relevant bond-length distributions. In contrast to a related study on $SrTiO_3$,[21] we chose not to include "soft" bond-length or bond-angle restraints in the refinement, in order to avoid the incorporation of any dynamical bias.[45]

The refinement process was allowed to continue until no further improvements in the fits to the data were observed. The real-space fits obtained for each of the five temperature points are illustrated in Fig. 2, where we have converted the

TABLE II. Distance window parameters $d_{\min}$ and $d_{\max}$ used in our $SrSnO_3$ RMC refinements and the corresponding mean pair separations $\bar{d}$ and their standard deviations σ at 930 K.

Atom pair	$d_{\min}$ (Å)	$d_{\max}$ (Å)	$\bar{d}$ (Å)	σ (Å)
Sr–Sr	3.5	4.6	4.06	0.21
Sr–Sn	3.0	4.0	3.52	0.16
Sr–O	2.2	3.8	2.84	0.28
Sn–Sn	3.7	4.5	4.06	0.13
Sn–O	1.8	2.3	2.06	0.10
O–O	2.3	3.4	2.89	0.22

experimental and modeled $T(r)$ functions to the related functions

$$D(r) = T(r) - 4\pi r\rho_0\left(\sum_m c_m b_m\right)^2 = 4\pi r\rho_0 G(r) \qquad (4)$$

for ease of representation.[42,43] The $F(Q)$ and Bragg profile functions were modeled similarly successfully, and the quality of these fits was just as consistent across the five data sets. As a final check of the quality of the RMC models, visual inspection of the configurations themselves showed the refinement to have proceeded without the inclusion of any anomalous regions of "damage" or unphysical atomic displacements.

C. Diffuse scattering calculations

Two-dimensional single-crystal diffuse scattering patterns were calculated from the RMC configurations using the method of Butler and Welberry[46] as implemented in the program EDRMC.[47] The approach separates the diffuse scattering pattern from the average structure of the atomistic configuration by calculating the diffuse structure factors

$$A(\mathbf{k}) = \sum_j \left\{ f_j(k) \sum_\ell \exp[i\mathbf{k}\cdot\mathbf{r}(j\ell)] - \langle F(\mathbf{k})\rangle \psi(\mathbf{k}) \right\}. \qquad (5)$$

Here, $\mathbf{r}(j\ell)$ is the position of each atom j in the unit cell ℓ, and $f_j(k)$ its scattering form factor (in our calculations here, we have used k-dependent electron scattering form factors). $\langle F(\mathbf{k})\rangle$ is the average unit cell structure factor and $\psi(\mathbf{k})$ is an interference function, given by

$$\psi(\mathbf{k}) = \prod_{\alpha\in\{x,y,z\}} \frac{\exp(ik_\alpha N_\alpha) - 1}{\exp(ik_\alpha)}, \qquad (6)$$

where the product is taken over each of the Cartesian axes $\alpha \in \{x,y,z\}$, along which the configuration box spans N_x, N_y, N_z unit cells.

The diffuse scattering intensities $I_D(\mathbf{k}) = A(\mathbf{k})A^*(\mathbf{k})$ are then averaged over a number of "subboxes" of the RMC configuration, a process which essentially serves to "blur" the scattering patterns by excluding long-range aperiodic correlations (these are generally found to introduce only high-frequency noise into the Fourier transform). In our calculations here, we have used a set of eight randomly selected subboxes, each of which corresponds to a $4\times3\times4$ supercell of the original orthorhombic unit cell.

Calculated average intensities $\langle I_D(\mathbf{k})\rangle$ were plotted for selected two-dimensional regions of reciprocal space, and the resultant images (which are produced using a constant intensity scale) were adjusted uniformly for sharpness, brightness, and contrast to maximize visibility of the diffuse scattering features wherever present.

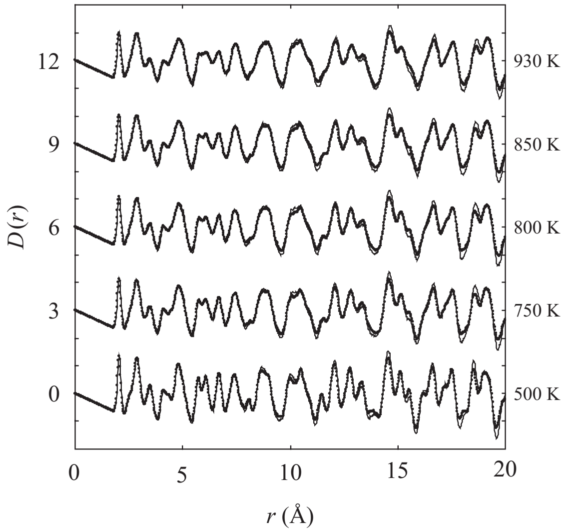

FIG. 2. Comparison of experimental $D(r)$ data (points) and refined fits (lines) for $SrSnO_3$ RMC configurations. Plots for successive temperature points have been raised by intervals of three units for ease of representation.

IV. RESULTS

A. Reverse Monte Carlo analysis

We begin our analysis of the RMC configurations by reporting some of the key bond-length distributions. The "bond lengths" calculated from average-structure determinations such as Rietveld refinement really only represent the separations between average atomic positions, which we might denote by the nomenclature ⟨A⟩–⟨B⟩. RMC refinement of total scattering data allows us to measure the true average bond lengths ⟨A–B⟩ because these correspond directly to peak positions in the experimental $T(r)$ function.

In this respect, the Sn–O1 and Sn–O2 functions are of particular interest because the average-structure values ⟨Sn⟩–⟨O⟩ decrease across the *Pnma*–*Imma* transition,[8] but we do not really expect there to be an actual decrease in Sn–O bond lengths with increasing temperature. The true average bond lengths ⟨Sn–O1⟩ and ⟨Sn–O2⟩ determined from our RMC models are shown in Fig. 3, together with their weighted average $\langle\langle \text{Sn–O}\rangle\rangle = \frac{1}{3}\langle \text{Sn–O1}\rangle + \frac{2}{3}\langle \text{Sn–O2}\rangle$; the distributions themselves are shown in Fig. 4(a). What is clear is that ⟨⟨Sn–O⟩⟩ increases smoothly across the transition, and that there is a slight difference in behavior of the Sn–O1 and Sn–O2 pairs. The Sn–O1 and Sn–O2 bond lengths appear almost identical in the *Imma* regime, suggesting a move to

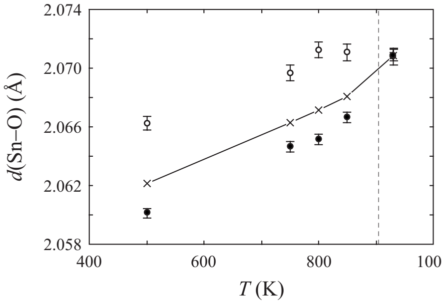

FIG. 3. Thermal variation in average Sn–O bond lengths as calculated from the $SrSnO_3$ RMC configurations. Open circles correspond to Sn–O1 bonds, closed circles to Sn–O2 bonds, and crosses to their weighted averages. The *Pnma*–*Imma* transition temperature is indicated by a dashed vertical line.

higher local symmetry in the $[SnO_6]$ octahedral geometries in this phase. While both bond lengths increase as the temperature is raised from 500 K toward T_c, ⟨Sn–O1⟩ stabilizes (and perhaps even decreases slightly) as the transition is approached.

The Sr–O1 and Sr–O2 bond-length distributions also become progressively more regular with increasing temperature [Fig. 4(b)]. The two distributions are quite different at 500 K, but the magnitude of this difference decreases continuously until, by 930 K, the two are almost identical. To some extent, this will reflect a reduction in the number of symmetry-inequivalent Sr–O1 distances (four in *Pnma* to three in *Imma*) and Sr–O2 distances (four in *Pnma* to two in *Imma*). The distributions are quite broad because there is actually a reasonably large spread in the various crystallographically distinct ⟨Sr–O1⟩ and ⟨Sr–O2⟩ separations; for example, at room temperature, these span the range 2.53–3.27 Å.

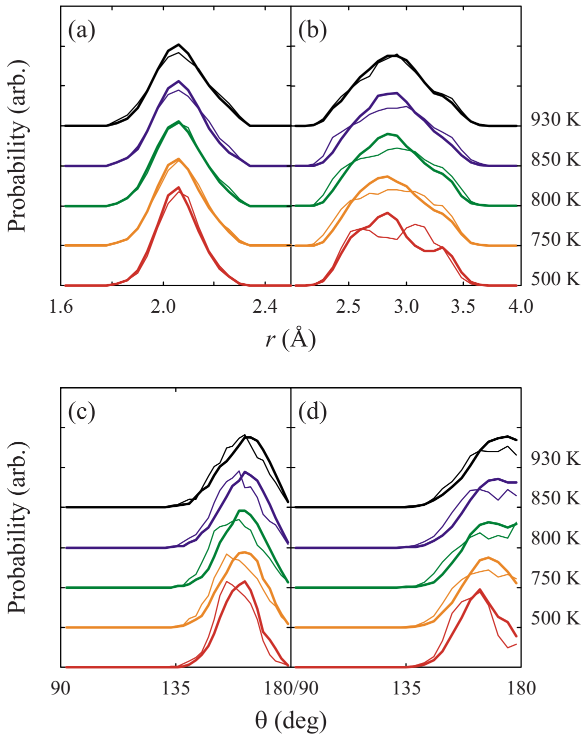

FIG. 4. (Color online) Upper panels: (a) Sn–O and (b) Sr–O nearest-neighbor distributions in the partial pair distribution functions. Lower panels: Sn–O–Sn bond-angle distributions as (c) raw probabilities $f(\theta)$ and (d) sine-weighted probabilities $f(\theta)/\sin\theta$. In all panels, fine and bold lines correspond to functions involving O1 and O2 atoms, respectively.

So both Sn–O and Sr–O bond-length distributions reflect an increasingly regular local structure as the *Pnma* phase is heated toward the *Pnma*–*Imma* transition: the $[SnO_6]$ octahedra become more uniform and the Sr–O bond lengths assume increasingly symmetric distributions.

In addition to the bond-length distribution functions, we were also able to calculate bond-angle distributions from our RMC configurations. The intraoctahedral O–Sn–O angles behaved much as might be anticipated in that the distributions—centered around 90° and 180°—simply broadened slowly with increasing temperature (data not shown). More interesting behavior was to be found in the interoctahedral Sn–O–Sn angles. The Sn–O1–Sn triplet corresponds to the linkage of $[SnO_6]$ octahedra roughly parallel to the crystallographic **b** axis (Fig. 1), and so its distribution is related to the tilt system parallel to the **a** axis. On the other hand, the Sn–O2–Sn triplets lie parallel to the (010) planes, and so their distribution reflects primarily the tilt system along **b**—the tilt system lost across the *Pnma*–*Imma* transition. It should be noted that the average Sn–O2–Sn angle is not constrained to be 180° in the *Imma* phase, but, nevertheless, its deviation from 180° should be somewhat smaller than in the *Pnma* regime (see Fig. 1).

The Sn–O–Sn distributions calculated from our RMC configurations are shown in Figs. 4(c) and 4(d), where they are given in two representations. One is the simple relative distribution function $f(\theta)$, which measures how often a given Sn–O–Sn angle is observed in the configuration. However, there is an intrinsic problem with $f(\theta)$ in that the number of angles around any value of θ is proportional to $\sin\theta$, so that it is impossible to obtain a peak around $\theta=180°$ even if the bond is fluctuating around this angle. A second representation, in which this problem is circumvented, is that of the function $f(\theta)/\sin\theta$. Both are included here because each one emphasizes slightly different features. For example, it is clear from the $f(\theta)$ distributions that the Sn–O1–Sn angle always deviates more strongly from 180° than the Sn–O2–Sn angle. Moreover, it appears that the maxima of both Sn–O1–Sn and Sn–O2–Sn distributions move closer to 180° at higher temperatures. Together with a concomitant broadening of the distributions, this means that the value of $f(\theta)/\sin\theta$ at 180° becomes significant for $T>750$ K. However, it would be difficult to conclude from these distributions alone whether the average Sn–O2–Sn angle at 930 K is indicative of an ordered *Imma* phase or of a disordered superposition of *Pnma* phases. To address this issue, we turn to geometric algebra, which enables a more sophisticated real-space analysis.

By comparing the orientations of $[SnO_6]$ octahedra within our RMC configurations to those of an ideal $Pm\bar{3}m$ configuration, it is possible to quantify the magnitude of octahedral

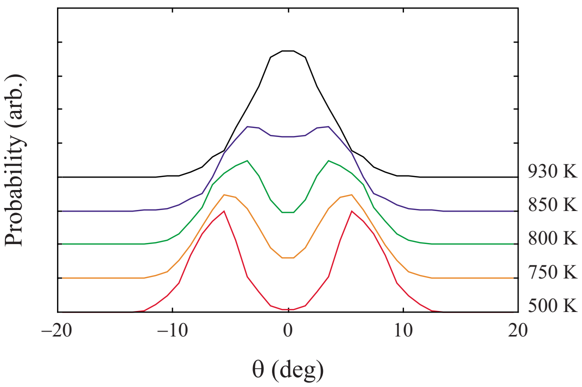

FIG. 5. (Color online) SnO_6 octahedral-tilt angle distributions calculated for rotations about the crystallographic **b** axis using GASP (Ref. 23).

tilts for each octahedron in the configuration about each of the crystallographic axes. To do this, we use a method based on geometric algebra,[48] as implemented in the program GASP.[23] For each octahedron, the program computes an associated "rotor"—an algebraic quantity whose components represent, to first order, the degree of rotation about the three Cartesian axes. The distribution function of these rotor components then reflects the distribution of octahedral tilt angles within the RMC configuration.

The calculated RMC tilt angle distributions corresponding to the **b** axis (the maxima of which should collapse onto 0° for a displacive description of the *Pnma*–*Imma* transition) are illustrated in Fig. 5. It is immediately apparent that the bimodal distributions in the *Pnma* regime evolve with increasing temperature into a unimodal distribution in the *Imma* phase. Tilt distributions calculated for the remaining two crystallographic axes showed the behavior expected of each—the **a** distribution was bimodal at all temperatures, the **c** distribution was unimodal, and both broadened appropriately with increasing temperature. The average tilt angles extracted from parity-corrected rotor values relative to the **a** and **b** axes (out-of-phase and in-phase tilt systems, respectively, with the former remaining present in *Imma*) are shown in Fig. 6. The values relative to **c** were found to be equal to zero at all temperatures, and so are not shown. Similarly, an average tilt angle of 0.02(4)° relative to **b** was calculated for the 930 K data, and hence was also equal to zero within error.

B. Three-dimensional diffuse scattering

Whether order-disorder or displacive in nature, the *Pnma*–*Imma* transition could give rise to a diffuse scattering intensity at primitive reciprocal lattice points in the *Imma* phase. We were interested in observing whether any evidence of such diffuse scattering could be discerned from our RMC configurations and, if so, what form it took in reciprocal space. We calculated diffuse scattering patterns for a number of reciprocal lattice planes according to the method described in Sec. III. A representative selection of these patterns calculated from the 500 K RMC configuration is shown in Fig. 7, where they are indexed according to the orthorhombic reciprocal lattice. What we found, entirely unexpectedly, was a rich system of diffuse features that took the form of intersecting rods parallel to each of the (primitive) reciprocal lattice vectors. Moreover, the structure of this diffuse scattering was unaffected by the *Pnma*–*Imma* transition, with the same patterns (with a subtle change in "reflection conditions"—discussed in more detail below) reproducibly calculated from each of our five RMC configurations.

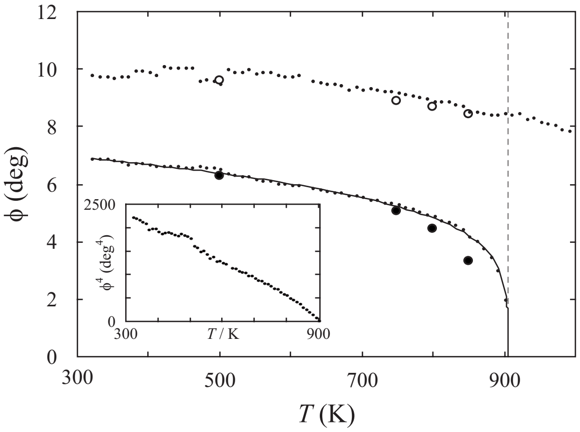

FIG. 6. Average octahedral-tilt angles ϕ calculated from the RMC configurations relative to the **a** (large open circles) and **b** (large filled circles) crystallographic axes. Values calculated from the anisotropic average-structure refinement described in Sec. V are shown as small points, and the guide-to-the-eye fit obtained using Eq. (7) is shown as a solid line. The dashed vertical line indicates the *Pnma*–*Imma* transition temperature, and the inset shows the temperature dependence of the fourth power of the in-phase tilt angle.

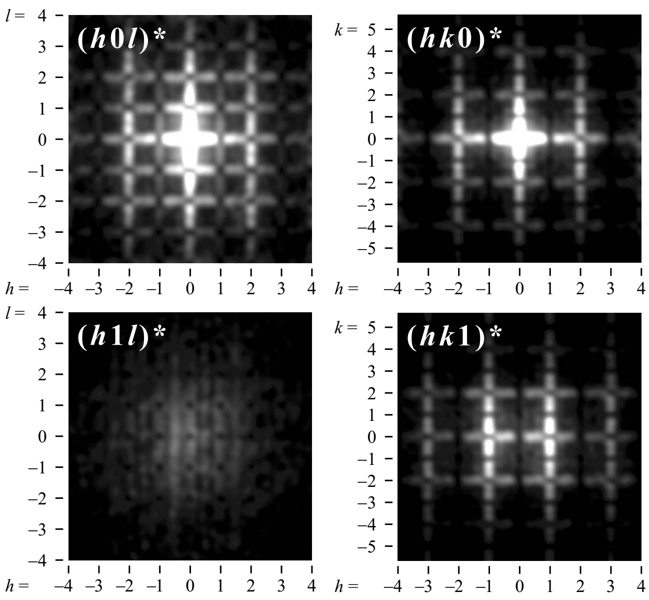

FIG. 7. Four representative diffuse scattering patterns calculated as described in the text from the 500 K $SrSnO_3$ RMC configuration. The basic form of these patterns was found to be almost entirely temperature independent.

Some clear reflection conditions emerge: the one-dimensional features parallel to $\mathbf{a}^*$, $\mathbf{b}^*$, and $\mathbf{c}^*$—i.e., $[h+\epsilon,k,l]^*$, $[h,k+\epsilon,l]^*$, and $[h,k,l+\epsilon]^*$—are observed only for $k=2n$, $h+l=2n$, and $k=2n$, respectively. These describe, for example, the absence of structured diffuse scattering within the $(h1l)^*$ plane (lower left-hand panel in Fig. 7), and along the $[1k0]^*$ and $[2k1]^*$ directions. The only qualitative variation in the scattering patterns observed to occur with increasing temperature was the additional condition $k+2l=4n$ for scattering parallel to $\mathbf{a}^*$ in the *Imma* (above 905 K) phase.

There does not appear to be any azimuthal variation in diffuse scattering intensities, which is a property often diagnostic of cation ordering processes in substitutionally disordered materials;[49] however, because there is no scope for cation ordering in a substitutionally ordered perovskite such as $SrSnO_3$, the absence of intensity variation implies a nontrivial relationship between scattering vectors and displacement mode eigenvectors. This is discussed in further detail below.

Finally, in order to confirm that these scattering patterns were not artifacts of the calculation method,[50] a series of artificial "correlationless" configurations was prepared with the same sets of atomic displacements as in the refined RMC configurations, but with these displacements assigned randomly throughout the configuration. Consequently, both the artificial and RMC configurations would possess precisely the same average structure (which indeed they did), but any local correlations present in the RMC model would now be destroyed. As expected, diffuse scattering patterns calculated from these new configurations were entirely featureless, and so the patterns revealed in Fig. 7 certainly reflect some real correlated process modeled during RMC refinement.

V. DISCUSSION

A. 905 K *Pnma*–*Imma* phase transition

Interpreting first the bond-length, bond-angle, and octahedral-tilt distributions reported above, it would seem that our RMC results cannot reasonably support an order-disorder description of the *Pnma*–*Imma* transition in $SrSnO_3$. The most convincing evidence is surely to be found in the octahedral-tilt distributions of Fig. 5, which show the same qualitative behavior as observed in $SrTiO_3$ across its well-studied displacive transition at 105 K.[21] The increase in local symmetry observed in the nearest-neighbor bond-length distributions also suggests a displacive transition; an order-disorder description would require a strong similarity in local structure between the two regimes.

While the GSAS refinements of Ref. 8 measured an apparent thermal decrease in the separation ⟨Sn⟩–⟨O⟩ between average Sn and O positions, our RMC analysis is able to measure the true average bond lengths ⟨Sn–O⟩ and their thermal expansion. Indeed, we calculate a positive average coefficient of thermal expansion of $0.92(9)\times10^{-5}\ \mathrm{K}^{-1}$, which, by way of comparison, is similar in magnitude to the value observed for Ti–O expansion in $SrTiO_3$ ($\alpha_{\mathrm{Ti-O}}=1.02(4)\times10^{-5}\ \mathrm{K}^{-1}$) in a previous RMC study.[21] The fundamental difference between ⟨Sn⟩–⟨O⟩ and ⟨Sn–O⟩ distances is attributable to the increased transverse vibrational motion of the O atoms relative to Sn…Sn vectors with increasing temperature, which allows the actual Sn–O bond lengths to increase while the crystallographic ⟨Sn⟩–⟨O⟩ separations decrease. This is a familiar and well-studied phenomenon, seen especially frequently in studies of silica polymorphs, e.g., quartz[51,52] and cristobalite,[53] but also to a milder extent in $SrTiO_3$.[21]

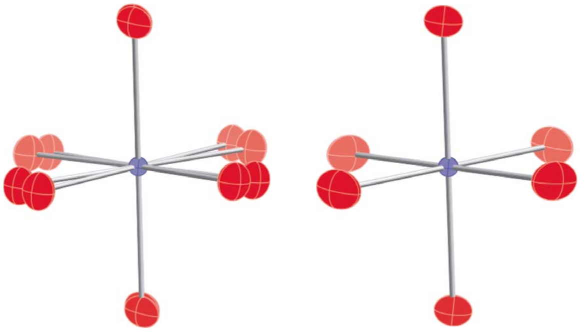

FIG. 8. (Color online) Comparison of $[SnO_6]$ octahedral geometries in (left) disordered *Pnma* and (right) ordered *Imma* average structural models of $SrSnO_3$, obtained by Rietveld refinement against the 923 K data of Ref. 8. Anisotropic thermal ellipsoids are drawn at 50% probability level.

In order to reconcile our octahedral-tilt distributions with the average-structure analysis of Ref. 8, we performed a new series of Rietveld refinements using the very same data, but employing anisotropic displacement parameters for all atoms. What we found was that the disordered *Pnma* model of the *Imma* phase gave thermal ellipsoids with significant spatial overlap, which effectively covered the same elongated scattering density as a single ellipsoid in the ordered *Imma* model (Fig. 8). Moreover, by allowing anisotropic displacement parameters in the ordered model, we produced better overall fits to the data than in the original disordered *Pnma* approach (which had used isotropic displacement parameters).

In Ref. 8, the variation of order parameter (defined in terms of the in-phase octahedral-tilt angles for the displacive model, and the difference in site occupancies for the order-disorder model) over the temperature range $0.357<T/T_c<1$ was fitted using an equation of the form

$$\phi(T)=\phi(0)[1-T/T_c]^{\beta}, \tag{7}$$

giving values of β equal to 0.187(2) and 0.160(5) for displacive and order-disorder models, respectively. These values are consistent with a rapid variation at temperatures close to T_c. With the new analysis in terms of a purely displacive transition, the order parameter is defined by the mean rotation of the SnO_6 octahedra. Plotting the fourth power of the angles calculated from our new structural refinements against temperature (inset to Fig. 6), we find a near linear relation, suggesting that the phase transition has tricritical behavior. Close to T_c, where we expect Eq. (7) to have physical justification, we see departures from the linear relation, which might imply a critical exponent of β of less than 1/4. However, it is known[54] that in tricritical phase transitions, there should only be logarithmic corrections to classical tricritical behavior (the critical dimensionality $d_c = 3$ for tricritical phase transitions), and we are not confident that the order parameter for temperatures close to T_c is not affected by the overlap of Bragg peaks as the peak splitting decreases. Thus, we conclude that the thermal behavior of the phase transition in $SrSnO_3$ is probably best described as a classical tricritical phase transition.

For completeness, a plot of the newly refined values of ϕ itself is given in Fig. 6, together with the RMC values and a guide-to-the-eye fit obtained using Eq. (7). It is worth noting that although the true value of β is probably equal to 1/4, we have allowed it to vary in producing this curve and have obtained the closest fit for $\beta = 0.208(1)$.

It is not known whether the *Pnma*–*Imma* transitions in related perovskites such as $SrZrO_3$, $SrRuO_3$, and $SrRhO_3$ also show tricritical behavior. To some extent, this issue has been obscured in the past by the assignment of the space group *Cmcm* instead of *Imma* to the higher-temperature phase (see, e.g., Refs. 16 and 17), and a *Pnma*–*Cmcm* transition (were it to occur) must be discontinuous.[7] Interestingly, the $I4/mcm$–$Pm\bar{3}m$ transition is tricritical in $SrZrO_3$,[16] suggesting that tricritical behavior may recur amongst this family of *Pnma*–*Imma*-$I4/mcm$–$Pm\bar{3}m$ perovskites; however, we note that the same transition is reported to be of second order in both $SrHfO_3$ and $SrRuO_3$.[55,56]

In summary, our RMC results suggest that a classical soft-mode picture is more reasonable than an order-disorder description of the *Pnma*–*Imma* transition in $SrSnO_3$. We find that the transition appears to be tricritical, and that the change in macroscopic symmetry is reflected in a substantially more regular local bonding environment in the *Imma* phase.

B. Ferroelectric nanodomains

We return now to the intriguing diffuse scattering patterns calculated from our RMC configurations. Their persistence across the *Pnma*–*Imma* transition clearly indicates an independence from the octahedral-tilt system involved in the transition. Indeed, it is straightforward to show that the *Pnma* phase does not support any low-energy octahedral-tilt modes other than at the Brillouin zone center; consequently, the off-center scattering must be due to some other mechanism. Because in our RMC configurations there is no scope for compositional disorder, the scattering must find its origin in some set of correlated atomic displacements.

The one-dimensional nature of the diffuse scattering parallel to each of the three orthogonal reciprocal lattice vectors indicates that these displacements are correlated in real space across planar regions perpendicular to each of the three crystallographic axes. Moreover, the reflection conditions provide information about the periodicity within these planes. Considering, first, the system parallel to $\mathbf{a}^*$, the condition $k = 2n$ implies that the displacements are periodic in real space along $\mathbf{b}/2$ and $\mathbf{c}$; the same condition for the $\mathbf{c}^*$ system implies a periodicity along $\mathbf{a}$ and $\mathbf{b}/2$. By calculating the diffuse scattering that arises from various pairs of atom types in the structure, we were able to show that only Sr, Sn, and O1 atoms contributed appreciably to the patterns of Fig. 7. What this means is that the displacement patterns must correspond to localized ferroelectric modes because the Sr and Sn atom positions repeat with the same real-space periodicity as the displacement pattern itself.

The scattering system perpendicular to $\mathbf{b}^*$ is characterized by a different set of reflection conditions; in this case, the condition $h + l = 2n$ implies a real-space periodicity given by the vectors $\mathbf{a}/2$ and $\mathbf{c}/2$ within planes perpendicular to $\mathbf{b}$. Again, these vectors correspond to the shortest Sn…Sr and Sr…Sr vectors within these planes, and so this third system also arises due to planar regions of correlated ferroelectric displacements.

In order to substantiate these conclusions further, we looked for real-space evidence of correlated ferroelectric displacements within our RMC configurations. Because the average Sn position is fixed by symmetry in both *Pnma* and *Imma* phases, we decided that Sn/Sn correlations would provide a particularly unambiguous handle on any correlated displacements, should they indeed exist. For each Sn atom (of which there are N, say) in a given RMC configuration, we calculated its displacement $\mathbf{u}$ from the average crystallographic site (while also accounting for any origin shift in the configuration), and used these values to determine the displacement correlation function

$$\eta(r) = \frac{1}{Nr^2} \sum \mathbf{u}(0) \cdot \mathbf{u}(r) \simeq \langle \mathbf{u}(0) \cdot \mathbf{u}(r) \rangle. \tag{8}$$

Here, we have taken the sum over all Sn pairs within planes perpendicular to a given crystal axis. A large positive value of $\eta(r)$ means the displacements of Sn atoms separated by a distance r are correlated within the given plane *and* occur in the same direction, while a negative value implies correlated motion in opposite directions, and a small value means any correlations are negligible.

In fact, this function is slightly complicated in that even for random displacements, $\eta(r)$ will peak at values of r that correspond to crystallographic separations—simply because any pair of atoms still separated by these special distances must have moved in similar directions. To distinguish this effect from the true correlations present, we calculated $\eta(r)$ functions not only for our RMC configurations, but also for artificial "disordered" configurations, in which the same set of Sn displacements had been distributed randomly throughout the lattice. The difference between these two functions provides a qualitative indication of the real correlated displacements refined by RMC; the three sets of functions calculated for families of planes perpendicular to each of the three crystallographic axes are shown in Fig. 9.

What we find is clear evidence of correlated ferroelectric displacements—and hence the existence of polar nanoregions—in that the difference functions are positive everywhere (within a very small margin). For each of the planar systems, the correlations appear to persist up to a maximum distance of approximately 10–15 Å. There do appear to be some minor variations in the strength and persistence

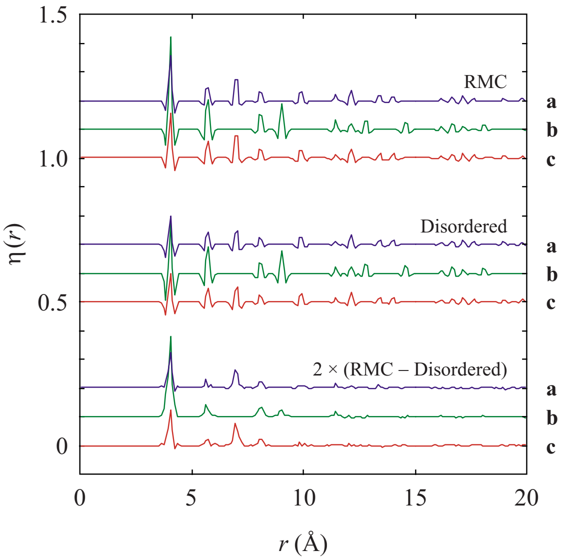

FIG. 9. (Color online) Sn displacement correlation functions $\eta(r)$, calculated for (top) RMC configurations and (center) disordered configurations as described in the text. The raw values have been offset by various constants in this representation. The difference between RMC and disordered $\eta(r)$ functions is shown in the bottom set of curves, where the values have been multiplied by a factor of 2 in order to aid visibility.

of correlations across the three planes, with the correlations strongest for planes perpendicular to **b**.

In order to understand better the real-space distributions of these nanoscale domains, we "marked" those Sn atoms whose displacements were sufficiently strongly correlated within a given planar system; the distributions obtained across some representative planes are shown in Fig. 10. The results seem to reflect well the conclusions of our previous analysis, in that the domains span regions approximately 10–15 Å in diameter and are correlated along the expected directions. Moreover, the density of correlated regions was greatest within the planes perpendicular to the **b** axis. All three domain types appeared to persist for only a single layer of octahedra along the direction perpendicular to the correlated plane; however, those regions of a given configuration found to be strongly correlated within one planar system were often also correlated within the other two.

Disappointingly, it did not appear that our RMC configuration gave a robust insight into the directions of the atomic displacements associated with the ferroelectric distortions. The average moment of Sn displacement was parallel to the vector [0.12, 0.98, 0.13], which suggests that Sn eigenvector might lie parallel to **b**; however, the extent of correlated motion along perpendicular directions was by no means negligible. It is possible that some of this information has been lost in the orientational averaging implicit in the original powder diffraction experiment—the absence of this information being suggested by the lack of azimuthal intensity variation in the diffuse scattering patterns of Fig. 7. One constraint is given by the additional *Imma* reflection condition observed for the scattering parallel to $\mathbf{a}^*$: the *Pnma*–*Imma* transition places each of the Sr, Sn, and O1 atoms on a mirror plane perpendicular to **a** (Fig. 1), and so the principal ferroelectric displacements within planes also perpendicular to **a** must be confined to this plane for the reflection condition to hold.

It is interesting to compare these results with previous reports of polar nanoregions in relaxor ferroelectrics such as PZN and PMN.[31,32,57] In fact, the single-crystal neutron diffuse scattering patterns observed in these materials are remarkably similar to those calculated from our $SrSnO_3$ RMC configurations. As a consequence, the proposed ferroelectric correlation pathways in these materials correspond precisely to the domains we have reported within planes parallel to the **a** and **c** crystal axes in $SrSnO_3$.

One obvious difference between the two systems lies in the corresponding correlation lengths: for PZN and PMN, the domains are thought to span regions up to about 100 Å in length,[32,57] in contrast to the 10–15 Å range observed here. Of course, we could not expect to observe such a large range in our $SrSnO_3$ configurations (the RMC box itself being only 45 Å wide), but our calculated value remains substantially less than the box limit, and so it is unlikely to be limited by the computational method.

The second difference lies in the number of *B*-site cations and the associated possibility of additional cation ordering processes in PZN and PMN. The Monte-Carlo-based analysis of Welberry *et al.* suggested that any link between *B*-site ordering and PNRs must have an incredibly weak effect on the diffraction behavior,[32] and indeed, the observation here

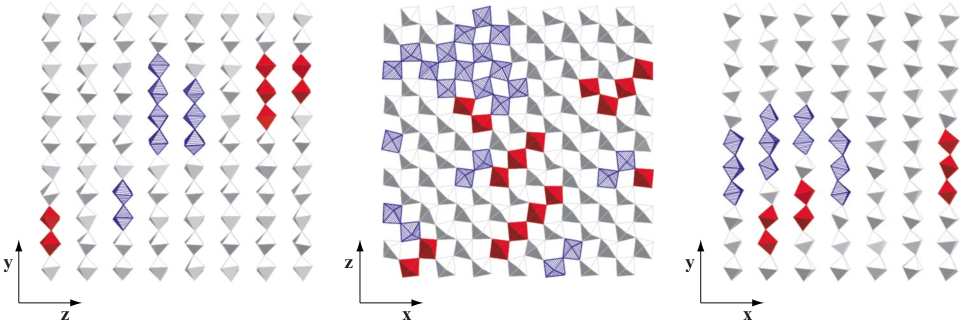

FIG. 10. (Color online) Ferroelectric nanoscale domains in our $SrSnO_3$ configurations perpendicular to the (left to right) **a**, **b**, and **c** crystal axes. $[SnO_6]$ octahedra in which the Sn displacement is strongly correlated with that of its neighbors are given in either solid red or striped blue representations, depending on the direction of the displacements.

of similar diffraction patterns in $SrSnO_3$ supports the independence of these two effects. In fact, it has been suggested elsewhere that cation ordering might be responsible for PNR formation in Pb-containing relaxor ferroelectrics[58,59]; obviously, this is not the case for $SrSnO_3$.

An alternative suggestion for PNR formation in PZN, proposed in Refs. 31 and 32, used a crystal-chemical argument based on "bond valence" calculations:[60] the apparent valence of Pb^{2+} ions was equal to 1.503 in their undisturbed crystallographic environments, but rose to a value of 2.002 after a set of proposed ferroelectric displacements was applied. A similar calculation for *Pnma* $SrSnO_3$ shows that the Sr^{2+} ions are slightly underbonded in the undistorted crystal structure, with a calculated bond valence equal to 1.79. Whether this degree of chemical "frustration" is sufficient to precipitate PNR formation is presumably a matter open to debate.

The observation of PNRs in $SrSnO_3$ suggests the material may, in principle, exhibit behavior related to that of the relaxor ferroelectrics,[26] although the temperature range over which PNR domain size is sufficiently large to produce the extremely high dielectric constants typical of true relaxors may lie well below those temperatures studied here. Indeed, the dielectric constant measured for a $SrSnO_3$ ceramic at room temperature was not especially high.[9] Perhaps of greater significance is the occurrence of PNRs at all within a family less-closely associated with relaxor behavior, and indeed in a system with no substitutional disorder. This is particularly important in the broader environmental context of producing effective Pb-free analogs of high-dielectric materials such as PZN and PMN. Interestingly, the relaxor properties of ferroelectric barium stannate titanate ceramics have recently been reported,[61] suggesting that stannates in general may offer a rich spectrum of ferroelectric behavior worthy of more detailed investigation.

VI. CONCLUSION

This study has shown the remarkable extent to which a combination of neutron total scattering and real-space atomistic refinement can yield valuable insight into a number of important local phenomena within crystalline materials. From within the same set of RMC $SrSnO_3$ configurations, we have extracted octahedral-tilt distributions that reflect the displacive nature of the *Pnma*–*Imma* transition at 905 K, together with the nature and distribution of planar ferroelectric domains and the associated real-space correlation functions. We have been able to resolve various issues raised in previous average-structure investigations of $SrSnO_3$, and, perhaps more importantly, have uncovered the unexpected ferroelectric properties of the material. These results present a paradigm in which to view the various applications of $SrSnO_3$ in electronic components and, indeed, for the structural and dynamical behaviors of the geologically important analog $MgSiO_3$.

ACKNOWLEDGMENTS

We acknowledge the provision of beam time from CCLRC (U.K.) and the financial support to A.L.G. from Trinity College, Cambridge.

---

[1] R. H. Mitchell, *Perovskites Modern and Ancient* (Almaz, Ontario, 2002).

[2] R. Comes, M. Lambert, and A. Guinier, Solid State Commun. **6**, 715 (1968).

[3] J. Hararda, J. D. Axe, and G. Shirane, Phys. Rev. B **4**, 155 (1971).

[4] N. Baskaram, A. Ghule, C. Bhongale, R. Muragan, and H. Chang, J. Appl. Phys. **91**, 10038 (2002).

[5] B. Zalar, V. V. Laguta, and R. Blinc, Phys. Rev. Lett. **90**, 037601 (2003).

[6] P. M. Woodward, Acta Crystallogr., Sect. B: Struct. Sci. **53**, 32 (1997).

[7] C. J. Howard and H. T. Stokes, Acta Crystallogr., Sect. B: Struct. Sci. **54**, 782 (1998).

[8] E. H. Mountstevens, S. A. T. Redfern, and J. P. Attfield, Phys. Rev. B **71**, 220102(R) 2005.

[9] W. Coffeen, J. Am. Ceram. Soc. **36**, 207 (1953).

[10] H. Wakana, S. Adachi, A. Kamitani, K. Nakayama, Y. Ishimaru, Y. Oshikubo, Y. Tarutani, and K. Tanabe, IEEE Trans. Appl. Supercond. **15**, 153 (2005).

[11] C. P. Udawatte, M. Kakihana, and M. Yoshimura, Solid State Ionics **108**, 23 (1998).

[12] C. P. Udawatte, M. Kakihana, and M. Yoshimura, Solid State Ionics **128**, 217 (2000).

[13] W. F. Zhang, J. Tang, and J. Ye, Chem. Phys. Lett. **418**, 174 (2006).

[14] M. Glerup, K. S. Knight, and F. W. Poulsen, Mater. Res. Bull. **40**, 507 (2005).

[15] B. J. Kennedy, C. J. Howard, and B. C. Chakoumakos, Phys. Rev. B **59**, 4023 (1999).

[16] C. J. Howard, K. S. Knight, B. J. Kennedy, and E. H. Kisi, J. Phys.: Condens. Matter **12**, L677 (2000).

[17] B. J. Kennedy, B. A. Hunter, and J. R. Hester, Phys. Rev. B **65**, 224103 (2002).

[18] B. J. Kennedy, K. Yamamura, and E. Takayama-Muromachi, J. Phys. Chem. Solids **65**, 1065 (2004).

[19] E. H. Mountstevens, J. P. Attfield, and S. A. T. Redfern, J. Phys.: Condens. Matter **15**, 8315 (2003).

[20] M. G. Tucker, D. A. Keen, M. T. Dove, A. L. Goodwin, and Q. Hui, J. Phys.: Condens. Matter **19**, 335218 (2007).

[21] Q. Hui, M. G. Tucker, M. T. Dove, S. A. Wells, and D. A. Keen, J. Phys.: Condens. Matter **17**, S111 (2005).

[22] Q. Hui, M. T. Dove, M. G. Tucker, S. A. T. Redfern, and D. A. Keen, J. Phys.: Condens. Matter **19**, 335214 (2007).

[23] S. A. Wells, M. T. Dove, and M. G. Tucker, J. Appl. Crystallogr. **37**, 536 (2004).

[24] R. L. McGreevy and L. Pusztai, Mol. Simul. **1**, 359 (1988).

[25] G. Burns and F. H. Dacol, Phys. Rev. B **28**, 2527 (1983).

[26] L. Cross, Ferroelectrics **76**, 241 (1987).

[27] G. Xu, P. M. Gehring, and G. Shirane, Phys. Rev. B **72**, 214106

(2005).

[28] G. Xu, Z. Zhong, Y. Bing, Z.-G. Ye, and G. Shirane, Nat. Mater. **5**, 134 (2006).

[29] P. Woodward and K. Baba-Kishi, J. Appl. Crystallogr. **35**, 233 (2002).

[30] W. Dmowski, M. Akbas, P. Davies, and T. Egami, J. Phys. Chem. Solids **61**, 229 (2000).

[31] T. R. Welberry, M. J. Gutmann, H. Woo, D. J. Goossens, G. Xu, C. Stock, W. Chen, and Z.-G. Ye, J. Appl. Crystallogr. **38**, 639 (2005).

[32] T. R. Welberry, D. J. Goossens, and M. J. Gutmann, Phys. Rev. B **74**, 224108 (2006).

[33] A. M. Glazer, Acta Crystallogr., Sect. B: Struct. Crystallogr. Cryst. Chem. **28**, 3384 (1972).

[34] Occasionally, the low-temperature phases are described in terms of *Pmcn* and *Incn* unit cells (Ref. 14) in which the in-phase tilt system occurs parallel to **a**, and the out-of-phase tilt system (not lost on transition to *Incn*) parallel to **c**.

[35] R. A. Cowley, Philos. Trans. R. Soc. London, Ser. A **354**, 2799 (1966).

[36] J. W. Benepe and W. Reese, Phys. Rev. B **3**, 3032 (1971).

[37] R. Kind, P. M. Cereghetti, C. A. Jeitziner, B. Zalar, J. Dolinsek, and R. Blinc, Phys. Rev. Lett. **88**, 195501 (2002).

[38] J. Chrosch, U. Bismayer, and E. K. H. Salje, Am. Mineral. **82**, 677 (1997).

[39] W. G. Williams, R. M. Ibberson, P. Day, and J. E. Enderby, Physica B **241-243**, 234 (1998).

[40] P. Day, J. E. Enderby, W. G. Williams, L. C. Chapon, A. C. Hannon, P. G. Radaelli, and A. K. Soper, Neutron News **15**, 19 (2004).

[41] A. C. Hannon, Nucl. Instrum. Methods Phys. Res. A **551**, 88 (2005).

[42] M. T. Dove, M. G. Tucker, and D. A. Keen, Eur. J. Mineral. **14**, 331 (2002).

[43] D. A. Keen, J. Appl. Crystallogr. **34**, 172 (2001).

[44] R. von Dreele and A. C. Larson, GSAS General Structure Analysis System, Los Alamos National Laboratory Report No. LAUR 86-748, 1986 (unpublished).

[45] A. L. Goodwin, M. G. Tucker, E. R. Cope, M. T. Dove, and D. A. Keen, Phys. Rev. B **72**, 214304 (2005).

[46] B. D. Butler and T. R. Welberry, J. Appl. Crystallogr. **25**, 391 (1992).

[47] A. L. Goodwin, R. L. Withers, and H.-B. Nguyen, J. Phys.: Condens. Matter **19**, 335216 (2007).

[48] S. A. Wells, M. T. Dove, and M. G. Tucker, J. Phys.: Condens. Matter **14**, 4567 (2002).

[49] R. L. Withers, Z. Kristallogr. **220**, 1027 (2005).

[50] The interference function $\psi(\mathbf{k})$ [Eq. (6)] has nontrivial values along each of the reciprocal lattice axes, and what this means is that the average scattering function $\langle F(\mathbf{k})\rangle\psi(\mathbf{k})$ can be significant at the same set of **k** points for which diffuse scattering was observed in our RMC configurations. While this contribution is rigorously accounted for in the diffuse scattering calculations and certainly should not give rise to artificial diffuse features, the precautionary calculations described here—in which an additional "correlationless" configuration with the same average structure as the RMC configurations [and hence, the same values of $\langle F(\mathbf{k})\rangle\psi(\mathbf{k})$] was used—show that the scattering does not arise from any spurious calculation effects.

[51] M. G. Tucker, M. T. Dove, and D. A. Keen, J. Phys.: Condens. Matter **12**, L723 (2000).

[52] M. G. Tucker, D. A. Keen, and M. T. Dove, Miner. Mag. **65**, 489 (2001).

[53] M. G. Tucker, M. D. Squires, M. T. Dove, and D. A. Keen, J. Phys.: Condens. Matter **13**, 403 (2001).

[54] A. Bruce, Adv. Phys. **29**, 111 (1980).

[55] B. J. Kennedy, C. J. Howard, and B. C. Chakoumakos, Phys. Rev. B **60**, 2972 (1999).

[56] B. J. Kennedy and B. A. Hunter, Phys. Rev. B **58**, 653 (1998).

[57] I.-K. Jeong and J. K. Lee, Appl. Phys. Lett. **88**, 262905 (2006).

[58] B. P. Burton and E. Cockayne, Phys. Rev. B **60**, R12542 (1999).

[59] B. P. Burton, E. Cockayne, S. Tinte, and U. V. Waghmare, Phase Transitions **79**, 91 (2006).

[60] N. E. Brese and M. O'Keeffe, Acta Crystallogr., Sect. B: Struct. Sci. **47**, 192 (1991).

[61] S. G. Lu, Z. K. Xu, and H. Chen, Appl. Phys. Lett. **85**, 5319 (2004).